The characterisation of a PID feedback-controlled array of TES-bolometers in a far-infrared double-Fourier interferometry testbed.

Chris S. Benson[a,b,*], Jeremy P. Scott[a], Locke D. Spencer[a], Rashmi V. Sudiwala[b,c], James Cox[c], Tyrone Jones[c], Berke V. Ricketti[a,d], David Naylor[a], Ken Wood[c], and Peter A. R. Ade[b]

[a]Institute for Space Imaging Science, University of Lethbridge, 4401 University Dr W, Lethbridge, Canada
[b]School of Physics and Astronomy, Cardiff University, Queen's Building, The Parade, Cardiff, Wales, UK
[c]QMC Instruments, Cardiff, Wales, UK
[d]Disruptive Space Technology Centre, RAL Space, STFC-Rutherford Appleton Laboratory, Didcot, UK

ABSTRACT

Double-Fourier interferometry (DFI) from a space-based platform provides a path to achieve broadband imaging spectroscopy in the far-infrared with sub-arcsecond angular resolution. To provide further study of the technique and improve its technology readiness, we have constructed a laboratory-based DFI testbed. This instrument is coupled to a custom array of 25 feedback-controlled transition-edge sensor (TES) bolometers. We present the results of characterisation experiments to optimise the detector system as an integrated component of the DFI assembly. We demonstrate that tuning the proportional-integral-derivative (PID) feedback control loops of the detectors and the timing of the multiplexed measurement process can modify the detector array's noise performance and speed of response to optical modulation for this purpose. From these, we have determined a set of optimised detector settings that reduce spectral noise in the spatial-spectral interferometer by 37–79%. In addition, we present further thermal characterisation of the detector array.

Keywords: Transition edge sensor (TES), terahertz detector, far-infrared, Fourier transform spectroscopy, time division multiplexing, instrument calibration

1. INTRODUCTION

Approximately half of the total energy density of electromagnetic radiation emitted by stars and accreting objects in the Universe throughout cosmic time, with the exception of the sun, is observed in the far-infrared (far-IR) regime (loosely defined as encompassing ∼30 to 1000 μm or 10 to 0.3 THz).[1,2] Since much of this spectral regime is largely inaccessible to ground-based observatories, the angular resolution of observations in the far-IR lags what has become readily available at wavelengths ranging from radio to X-ray. The development of a far-IR double-Fourier interferometer (DFI) from a space-based platform has been identified by the astronomical community as having substantial potential to open up the far-IR to sub-arcsecond imaging spectroscopy.[3–10]

To provide further study of the double-Fourier technique and to build towards a future space-based far-IR interferometer, we have developed a laboratory-based DFI operating within a spectral band of 200–2200 GHz. The DFI is coupled to a unique array of feedback-controlled transition edge sensor (TES) bolometers. In this paper, we present and discuss the characterisation of this TES array and its optimisation for use as a detector system for the DFI testbed. This investigation has led to a 40–70% reduction in the spectral noise of measurements made with the interferometer.

*Send correspondence to C.S.B.: E-mail: BensonC@cardiff.ac.uk

1.1 TES Bolometer Theory

The voltage response of a bolometer to a change in optical load can be written,[11–13]

$$S_V = \frac{I_{\rm bias}\alpha R_{\rm TES}(T)}{TG_e}\frac{1}{1+i\omega_s\tau_e}, \tag{1}$$

where ω_s is the small signal oscillation in observed light, T is the temperature of the detector, $R(T)$ is the electrical resistance of the thermometer, I is the bias current to the thermometer, and τ_e is the detector's effective time constant. In Eq. 1, $\alpha = (T/R)dR/dT$ is a unitless measure of the steepness of the superconducting transition of a TES evaluated at the steady-state temperature of the detector. The parameter $G_e = G - P_{\rm TES}\alpha/T$, where $P_{\rm TES}$ is the electrical power dissipated in the thermometer, used in Eq. 1 is an effective thermal conductance which accounts for electrothermal feedback.[11] For TES bolometers, $\alpha > 0$ and it is possible for G_e to reach zero resulting in thermal runaway.[11] For this reason, it has become common to operate the TES thermometer in a constant-voltage bias such that its Joule heating decreases as its temperature (and thereby its resistance) increases under an optical load.[12,13] When operating under a constant-voltage bias, changes in the current through the TES are often sensed and amplified using a superconducting quantum interference device (SQUID).[3,11,13]

1.2 Feedback-controlled TES bolometers

The 5x5 TES detector array that is coupled to the DFI instrument, provided by QMC instruments (Cardiff, Wales), operates with detectors in an approximately constant-current biased state contrary to the usual constant-voltage biased operation. These detectors do not employ electrothermal feedback to maintain the operation of the bolometers about the superconducting transition of the thermometer. Instead, detectors in the QMC TES array make use of an actively controlled heating element and a proportional-integral-derivative (PID) feedback loop to maintain the operating point of the detector within a carefully timed multiplexing loop. The operation of the detectors is read out and maintained by a National Instruments field programmable gate array (FPGA) which multiplexes 4 simultaneous channels (A-D) switching through 7 rows in time (0-6, see Fig. 1). Thermal and electrical diagrams of a single detector in the array are shown in Fig. 2. Operation about the set temperature on the superconducting transition of the TES is achieved by balancing the thermal conduction to the surrounding environment of the cryostat, the optical loading on the detector, the Joule heating from the bias circuitry of

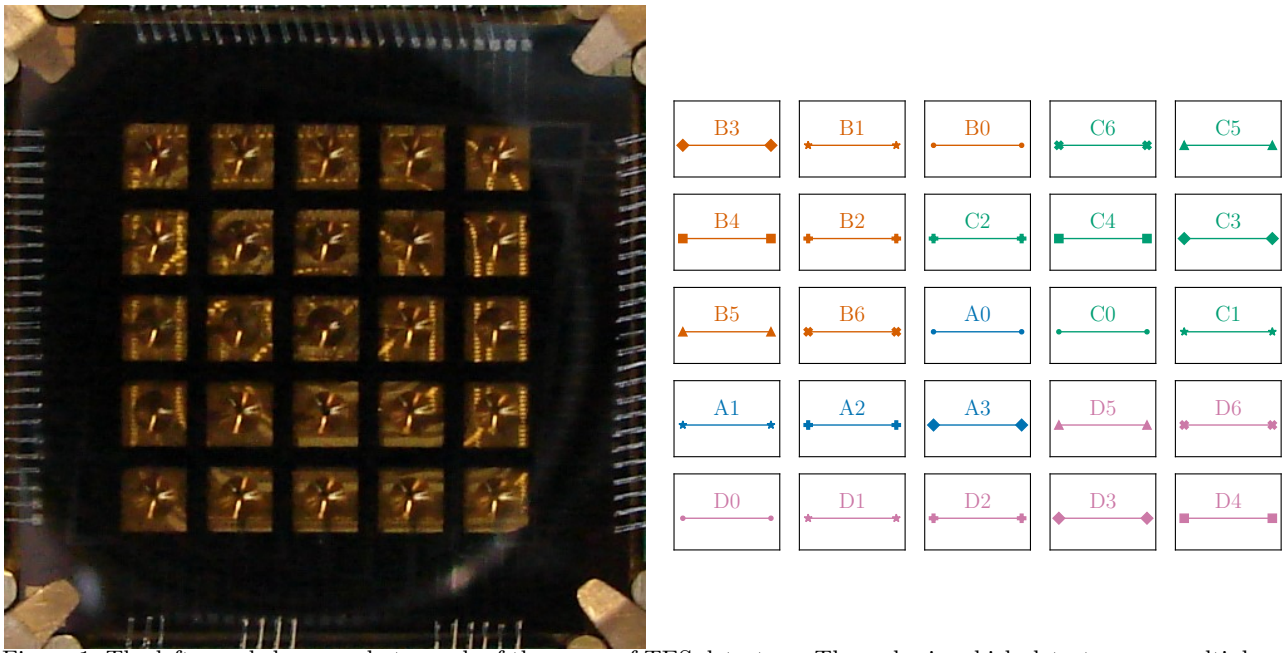

Figure 1. The left panel shows a photograph of the array of TES detectors. The order in which detectors are multiplexed by the FPGA readout system is outlined in the right panel.

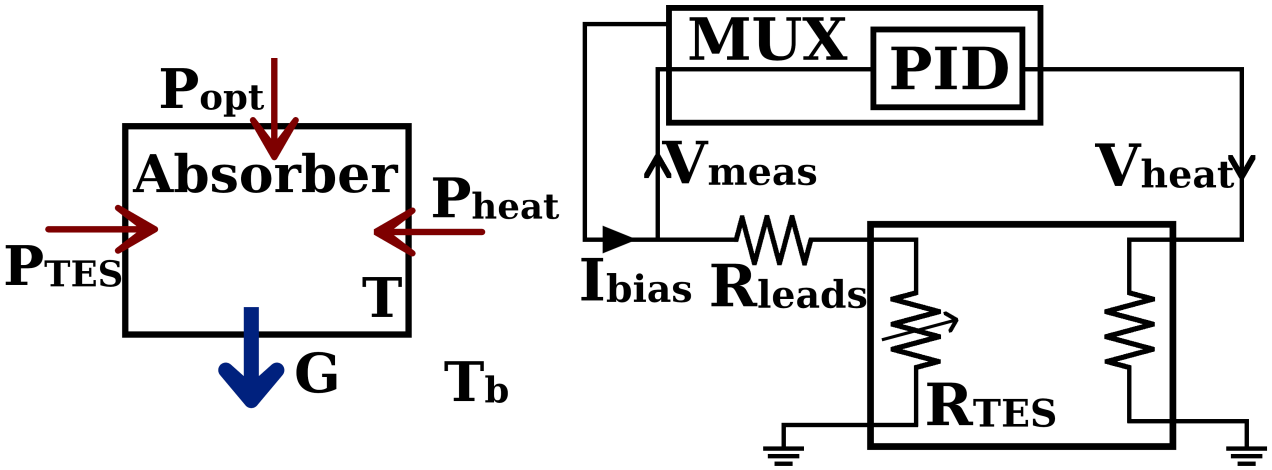

Figure 2. A simplified thermal (left) and electrical (right) diagram of a single feedback-controlled TES bolometer in the array. The multiplexing (MUX), PID control, and detector bias are achieved through a combination of warm electronics and an FPGA.

the TES, with the feedback-controlled heating element. Under an increase in incident optical power, there is a change in the TES temperature state that is measured by the voltage across the TES ($\mathbf{V_{TES}}$). In response, the PID feedback loop calculates the necessary reduction in heater power to maintain the setpoint at the specified time within the multiplexing cycle. In this way, the heater power provides a measure reciprocal to the optical loading on the TES detector. The steady-state power balance of a detector follows that of a typical bolometer with the addition of the heater power,

$$C_a \frac{dT}{dt} = P_{\text{elec}} + P_{\text{opt}} + P_{\text{heat}} - P_{\text{bath}} \quad [\text{W}], \tag{2}$$

where C_a is the lumped heat capacity of the detector and each P-term is the power provided or dissipated by the electrical bias to the thermometer, the optical loading on the detector, the heating element, and thermal conduction to the cryogenic environment. Also due to this operation, the response of a given detector (i.e., Eq. 1) is modified by the transfer function of the PID controller. Through this configuration, the detector array makes use of traditional amplifiers rather than a SQUID-based readout solution while also maintaining sufficient sensitivity for use in room-temperature far-IR/THz instruments with the detectors operating within a $\sim$4 K environment (having optically measured noise equivalent powers of $\sim 5 \times 10^{-12}$ W/$\sqrt{\text{Hz}}$).[14] Additionally, this operation is highly customisable providing a versatile detector system that can be optimised for specific use cases.

In Spencer et al. (2022),[15] we presented the operation of the detector system, its readout, and its multiplexing configuration. Additionally, we provided an early exploration of its adjustable parameter space. Since these initial writings, the detector system has been successfully commissioned and integrated into the DFI testbed and can be more fully tested and optimised within the context of the DFI.[16,17]

2. DETECTOR OPTIMIZATION

Owing to the timing of the multiplexing and feedback processes involved in a detector measurement, the detectors under study do not maintain constant operation on their superconducting transition. Instead, a detector's thermal state switches between superconducting and normal conducting states throughout a single measurement and remains within its superconducting state while other detectors in the array are measured. The exact timing of the measurement process and the response of a given detector are governed by a set of user-adjustable parameters.

The adjustable parameters that modify detector behaviour can be divided into two categories: parameters that adjust the timing of the multiplexing process and parameters that tune the PID control of a single detector. Detector timing parameters can be used to adjust (1) the length of a measurement pulse, (2) the duty cycle of

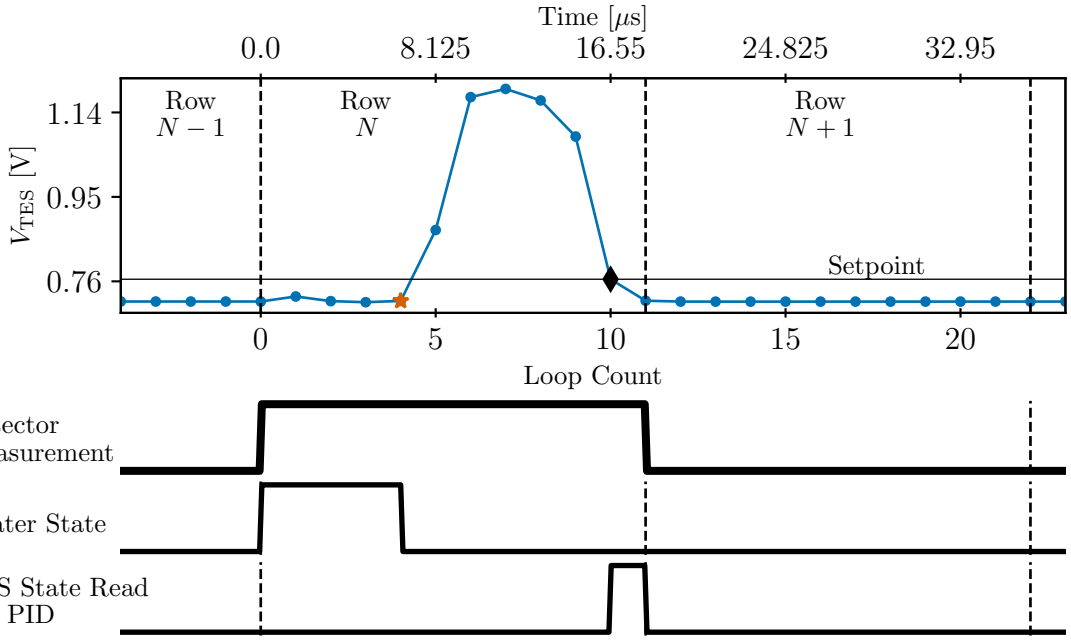

Figure 3. An example of a single detector measurement pulse within the multiplexing cycle. When the the row of the detector (N) is switched to, the TES heater becomes active for 6.5 μs at the start of the measurement pulse, the TES state is measured for use in the PID 16.25 μs after the start of the pulse, and the detector is inactive and no longer biased after 18.03 μs having completed a full detector measurement pulse. The cycle then switches to another detector row ($N + 1$). The PID setpoint has been marked by the horizontal line. The heater switch-off point is marked by a star while the TES state measurement for PID calculations is marked by a diamond.

the heater within a measurement pulse, and (3) when within a measurement pulse the TES state is measured for use in the PID feedback. A measurement pulse is divided into "loop counts" that correspond to a counter which increments when a measurement of the TES state or another operation can be completed by the FPGA. The time at which the heater switches off (having switched on at the start of a detector measurement) and the time when a TES measurement is used in PID feedback are set to occur on a given loop count. In the example shown in Fig. 3, the heater is chosen to switch off on a loop count of 4, the TES state is measured for use in the PID on a loop count of 10, and the detector is inactive from loop count 11 onward (i.e., the pulse width is 11 loop counts). As these timing parameters define the multiplexing process, they are ubiquitous across every detector in the array. When the multiplexing cycle is turned off, the measurement cycle remains on a single row (i.e., the row counter in Figure 3 does not increment).

Each detector is read out and maintained by a dedicated PID calculation,

$$u(t) = K_P e(t) + K_I \int_0^t e(t')dt' + K_D \frac{d}{dt} e(t) \quad \text{[a.d.u]}, \tag{3}$$

where $u(t)$ is the output signal from the PID calculation and $e(t)$ represents an error signal from the desired state or setpoint. The proportional, integral, and derivative terms of Eq. 3 all have an associated gain or weighting factor, K_P, K_I, and K_D, respectively. The PID setpoint and associated gains can be adjusted on a per-detector basis.

2.1 Thermal characterization

The sensitivity of the PID feedback for a detector is increased by choosing a setpoint which occurs on the steepest part of the transitions (i.e., where α is at its maximum). As such, we expect that choosing the PID setpoint accordingly will increase detector performance. We measured the superconducting transitions of the detectors in situ by monitoring the TES voltage while the cryostat was allowed to warm to a point at which all detectors

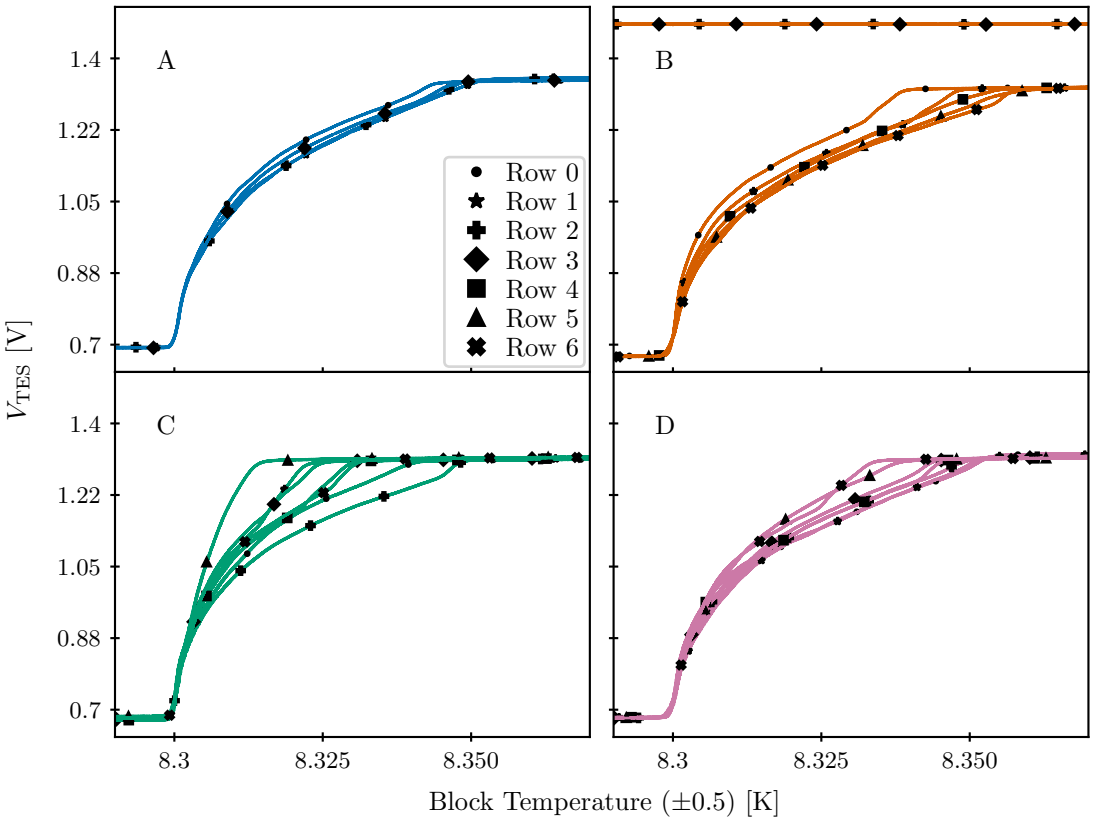

Figure 4. The superconducting transitions of each active detector in the array separated by multiplexing channel.

had passed through their transitions. A mirror was placed at the input to the detector cryostat effectively reducing the optical loading on the detectors (i.e., the detectors see themselves at ∼8 K with minimal emission from the reflective room-temperature mirror). The temperature of the cryostat environment was monitored using a diode thermometer located on the detector block. These transitions are shown for the entire detector array in Fig. 4. The calibration of the diode thermometer is such that there was a ±0.5 K uncertainty in the absolute temperature of the cryostat environment. The statistical uncertainty in temperature measurements was estimated to be ±30 mK from repeated measurements while the cryostat warmed from ∼6 to ∼11 K.

Due to noise in measurements of the TES state (having a 2.8 mV standard deviation), the derivative of the superconducting transition was determined from a smoothed spline fit to the curve. This is shown for the central detector in the left panel of Fig. 5 showing a maximum value $\alpha = 687 \pm 5$ at a TES voltage of ∼0.722 V.

When measuring the superconducting transitions, we noted that operating the detector array without multiplexing showed a much steeper transition than when measured in standard multiplexing mode. We attribute this to self heating of the detectors from the bias circuitry resulting in poor thermalisation between an individual detector and the detector block (see Benson 2024[14]). We note that the superconducting transition of the central detector that we measured and presented in Spencer et al. (2022),[15] did suffer from self heating. The results presented here provide a more accurate measurement.

Though we have not been able to provide a full thermal characterisation of the detectors through in situ measurements with our current test equipment, we have obtained a measurement of the dynamic thermal conductance, $G = dP/dT$, for each detector. This is often determined by measuring the power needed to bias the TES at various bath temperatures.[13,18] This could also be achieved in practice through the use of a heating element on the absorber of each TES to obtain different static temperature conditions as in Karwan et al. (2008).[19] Due to the biasing arrangement of the TES thermometers in our system, the bias circuity to the TES is a

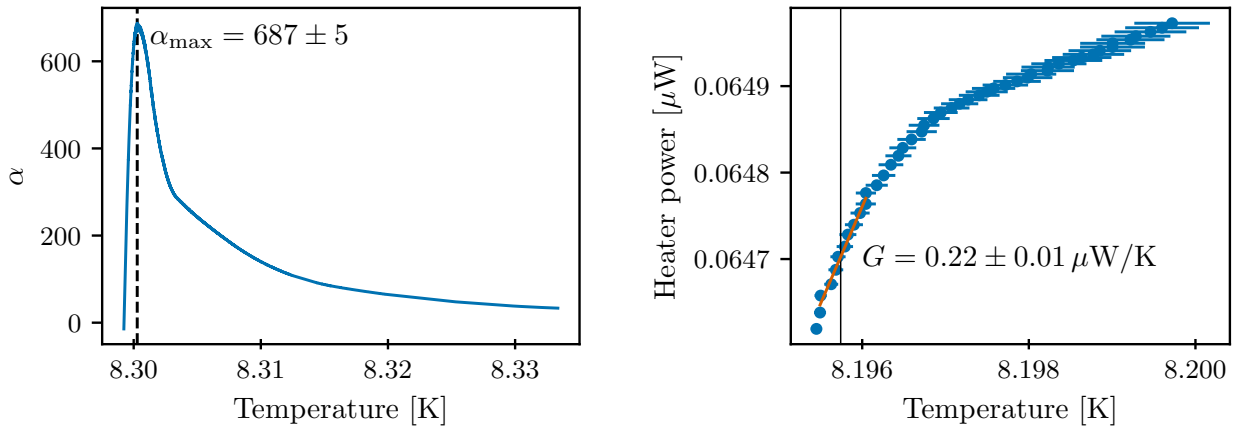

Figure 5. The steepness of the superconducting transition of the central detector determined from a cubic spline fit of the measured curve is shown in the left panel. The right panel demonstrates the dynamic thermal conductance determined for the central detector.

Table 1. The maximum value for α measured from the superconducting transition of each detector in the array. The corresponding voltage values of the TES at the steepest point are also provided.

Detector	V_{TES} [V]	$\alpha_{\max}$	Detector	V_{TES} [V]	$\alpha_{\max}$
A0	0.722	687 ± 5	C3	0.737	$1\,162 \pm 6$
A1	0.735	882 ± 5	C4	0.726	$1\,192 \pm 6$
A2	0.770	743 ± 4	C5	0.739	$1\,164 \pm 6$
A3	0.733	879 ± 5	C6	0.739	880 ± 5
B0	0.720	$1\,305 \pm 7$	D0	0.734	697 ± 4
B1	0.743	890 ± 5	D1	0.731	702 ± 4
B4	0.735	739 ± 4	D2	0.725	779 ± 4
B5	0.732	565 ± 3	D3	0.722	928 ± 5
B6	0.741	633 ± 3	D4	0.726	$1\,033 \pm 5$
C0	0.730	916 ± 5	D5	0.748	764 ± 4
C1	0.731	$1\,023 \pm 5$	D6	0.752	713 ± 4
C2	0.736	885 ± 5			

significant source of self-heating and the detectors require the PID multiplexing arrangement to prevent thermal runaway. This makes measurements after this fashion impractical. Instead, we have employed a technique similar to the second method performed by Karwan et al. (2008)[19] in which a small change in heater power and the corresponding change in TES temperature is monitored. In this way, G is measured directly as $G = \Delta P_{\mathrm{heat}}/\Delta T$. For our system, the change in detector temperature is controlled by changing the setpoint of the PID and the heater power required to maintain the setpoint is monitored.

For the detector to maintain a set temperature in the steady state, it is required that Equation 2 holds for input and output sources of thermal power in a sufficiently long time average. Provided that the time average of optical loading and electrical bias is constant, the change in the power-loading of the detector is given by, $\Delta P = \Delta P_{\mathrm{heat,avg}}$. Since the heater is only active for the specified duty cycle while conduction occurs continuously, $G = 0.4\Delta P_{\mathrm{heat}}/\Delta T$ for a detector operating with a pulse width of 10, a blanking time of 4, and without multiplexing.

Fig. 5 shows thermal conduction measurements for the central detector. During this measurement, the heaters corresponding to each of the other detectors have been manually switched off and the detectors are not multiplexed to avoid deleterious thermal and electrical cross-talk.[14] To minimize changes in the optical load throughout measurements, a mirror was placed at the cryostat window. In the more sensitive lower region of the transition, the dynamic thermal conduction of the central detector remains at a constant value of $0.22 \pm 0.01\,\mu$W/K. We found that the repeatability in measurements of the superconducting transition to be the dominant source of uncertainty in our conduction measurements (see also Benson 2024[14]).

2.2 Low frequency detector noise

The modulation frequency of light, f, incident on a detector in a DFI follows that of a standard FTS,[20,21]

$$f = mv\sigma, \tag{4}$$

where v is the speed of the moving mirror, σ is the spectral frequency of observed light given in wavenumbers (i.e., $\sigma = 1/\lambda$, where λ is the wavelength of light), and m is a folding factor which depends on the optical configuration of the DFI.[21] For the Mach-Zehnder layout of the DFI, $m = 4$. Thus, in FTS measurements the measured optical modulation can be chosen to occur over a signal band for which the detectors experience less noise by choosing an appropriate speed of travel for the moving mirror.

To measure the noise spectrum of detectors in the array (in signal frequency space), a mirror was again placed at the cryostat window to reduce optical loading and provide a static optical field. The resulting noise spectra from the central detector and an off-axis detector are shown in Fig. 6. The noise spectrum of each detector demonstrates that they are dominated by $1/f$-noise at signal frequencies lower than $\sim$5 Hz. We have found the detectors to be sensitive over an optical spectral band of 250–2200 GHz (see Benson 2023[17]), thus the minimum travel speed for the moving mirror should be chosen to be greater than 0.7 mm/s to ensure that the modulated signals measured by the detectors fall within the white noise band. The maximum travel speed of the moving mirror is dictated by the detector array's response speed (i.e., the effective time constants of the detectors). This can be adjusted for the detector system through the suite of user-adjustable parameters (see §2.3 and §2.4).

2.3 Detector timing

We have demonstrated in Spencer et al. (2022)[15] that the noise performance of a detector can be improved through modifications to the timing of the detector measurement process in the multiplexing cycle (noted earlier within this section, also see Fig. 3). The three adjustable timing parameters are set in the control software as a number of loop counts. Through measurements of a static optical load, we have found that pairing a heater activity time of 17 μs (10 loop counts) with a delay of 8.3 μs (5 loop counts) after the heater switches off improves the noise performance of the central detector by a factor of $\sim$1.7.[14,15]

Since the goal of the detector system is to measure optical modulation from the DFI, we have also studied the effects of changes to the timing of the detector measurements on the effective time constant of the central detector. A Toptica TERASCAN 1550 continuous wave photomixer was used as a THz source with a mechanical chopper to measure the response of the detectors to modulation up to $\sim$1 kHz.[22] These results are shown in

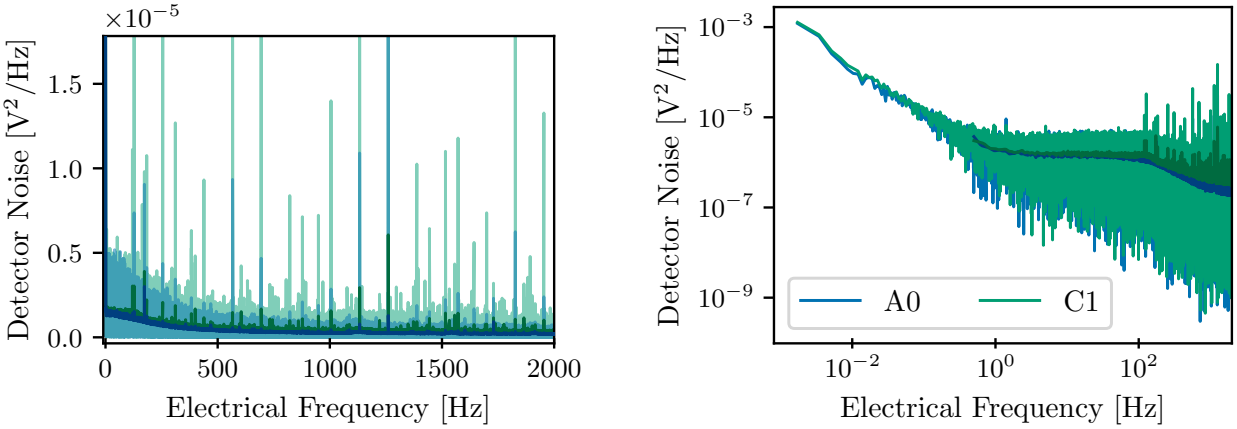

Figure 6. Detector noise spectra corresponding to a central and an off-axis detector are shown over linear (left) and logarithmic (right) axes. In both panels, the darker curves show the spectra smoothed by a Hann filter.

Fig. 7. Increasing the time that the heater remains active results in a change in the power required to maintain the PID feedback causing a natural offset in the response curves shown in Fig. 7. Increasing the total time required to measure a detector allows for greater durations of heater activity and longer TES state read delays to be accommodated resulting in a slower detector response (as expected). To accommodate full Nyquist sampling of measurements over the full spectral band of the DFI, a total detector measurement time of less than 12.9 μs (12 loop counts) is needed. With this total measurement time, a heater activity time of 6.4 μs (6 loop counts) and a TES read delay of 11.8 μs (11 loop counts) can be accommodated to reduce detector noise.

2.4 PID tuning

Through PID tuning, both the response speed and noise properties of each detector can be optimised for use with the DFI. These effects are shown for the central detector while viewing a blackbody source chopped at 30 Hz averaged over several thousand periods of the chopped source in Fig. 8.[15] It is evident that over this parameter range, increasing the proportional-term (P-gain) has a slight effect on the amplitude decreasing by 5.8% at the highest P-gain of 3 000 data units. Additionally, the integral gain (I-gain) has a dramatic effect on the ability of the detector to respond to optical modulation with a gain of 100 data units being near the limit of sufficient response at 30 Hz. Varying the derivative gain appears to have little effect on the output signal in the observed cases. Fig. 9 demonstrates that for a variety of proportional and integral gains, the derivative term increases the noise of the system in general. These measurements, coupled with those of a modulated optical load signal (see Fig. 8), suggest that the inclusion of the derivative term of the PID loop degrades detector performance.

To estimate the signal-to-noise ratio (SNR) of the detector, we measured the effects of P- and I-term weighting the PID feedback of the central detector while viewing a 90°C blackbody modulated by a chopper at 40 Hz. Figure 10 demonstrates these results for a range of P- and I-term gains. The SNR of the detector with respect to broadband detector noise has been estimated by comparing the amplitude of the average chopped profile from several hundred periods of the chopper to the residual of the average profile on a per-chopper period basis. Detector SNR from this metric is shown in the left panel of Fig. 10. The SNR measurements by this metric coupled with the noise measurements of a static optical load suggest that broadband noise is reduced at low P- and I-term gains as the detector is less responsive to high-frequency noise. This represents a factor of ∼3 improvement in broadband SNR over the default PID parameters.

To estimate the SNR of the central detector in a frequency band local to the chopped signal from the blackbody, we considered the power spectral density of the detector timeline. The detector signal has been determined as the integral over a 20 Hz signal bandwidth centred on the frequency of the spectral peak of the chopped frequency in the detector measurement time series. Noise has been estimated as the signal from the power spectrum of the detector while viewing a static optical field provided by a mirror (under the same PID

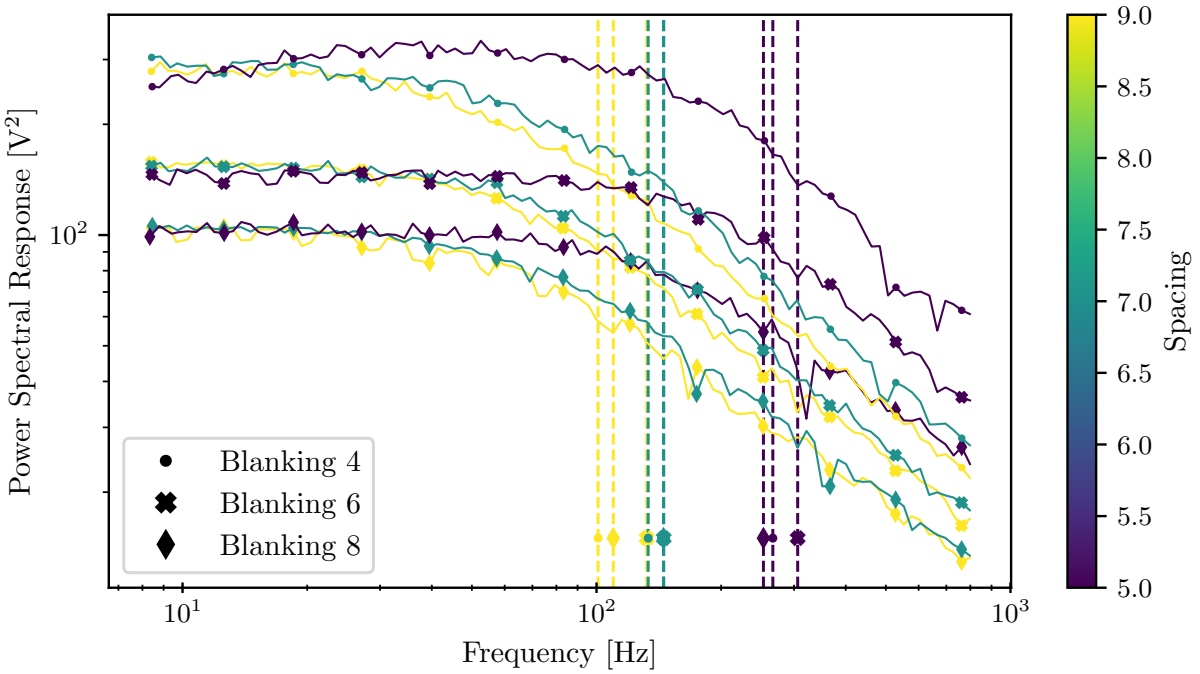

Figure 7. The frequency response of the central detector operating with a variety of detector timing parameters. The dashed vertical lines indicate the −3 dB frequency cutoff of each response curve. Colour shows the number of loop counts between the heater switch-off and the read index (spacing) while different markers indicate the blanking time. Each measurement was made with a pulse width set to be one greater than the read index such that the read index is the last loop count of a measurement pulse.

conditions) integrated over the same frequency band. These measurements are shown in the right panel of Fig. 10. There is a localised range of P- and I-term gains for which the SNR in a frequency regime local to the signal from the chopped blackbody is improved by a factor of ∼2.6 over default parameters.

Fig. 8 has demonstrated that PID tuning can have a dramatic effect on the response of a detector and that the weight of the I-term plays a dominant role in this. To study the effects of PID tuning on detector response, we have measured the central detector response under a variety of PID conditions. Fig. 11 shows a summary of P-term and I-term tuning on the effective time constant of the central detector. We have obtained these through a least-squares fit following the form of Equation 1 to the detector's response while viewing the photomixer source with a chopper. These demonstrate that detector response speed is improved by a high weighting of the I term coupled with a low weighting of the P term. In all cases, an I-term gain of 10 data units results in a high uncertainty in the fitted detector time constant as the PID control of the detector results in deviations from the response profile of a more typical bolometer. The value of χ^2_{red} provides a goodness of fit metric for regions in PID space in which the detectors deviate from the low-pass response of the fitted equation and demonstrated that response profiles within desirable regions of proportional and integral term weighting are sufficiently modelled by the fit equation.

2.5 Spectral noise

Balancing the detector time constant requirements for the interferometer operating in a 250–2200 GHz spectral band and improvements to detector noise performance, we have determined a set of better-optimized detector parameters to reduce the noise in spectral measurements of the DFI made with the central detector of the array (see Tab. 2).

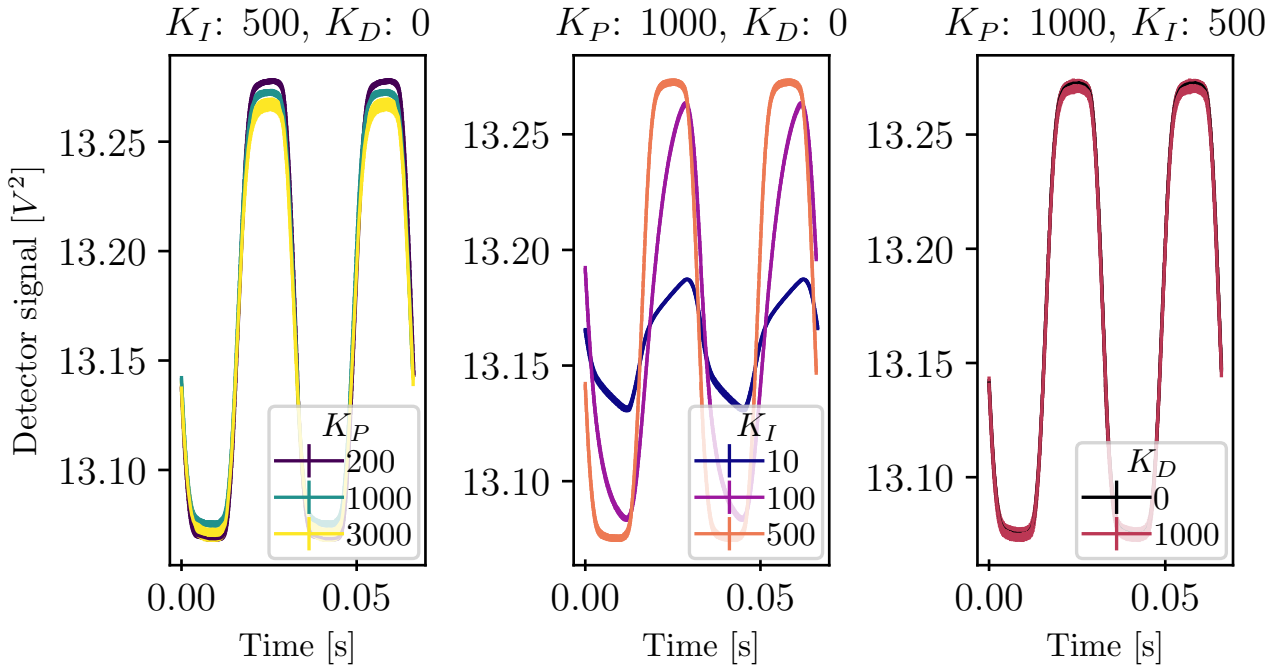

Figure 8. The average central detector output signal while viewing a chopped blackbody source under a variety of PID conditions.

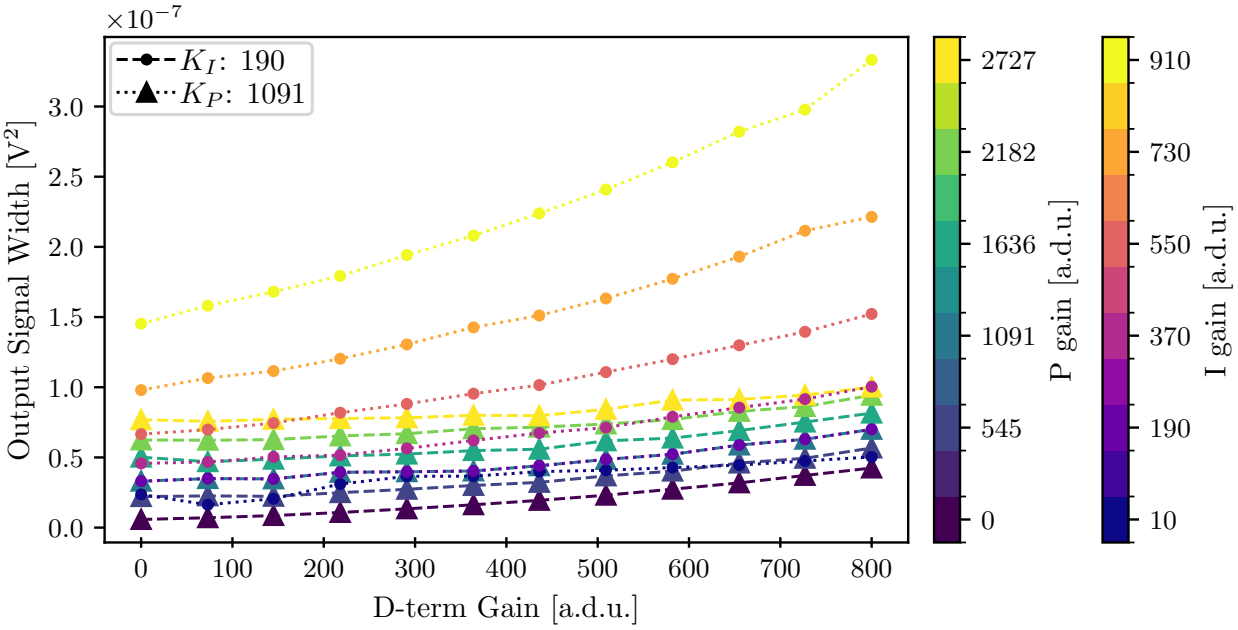

Figure 9. The effect of increased derivative-term weighting in the PID loop on the noise distribution of the central detector while viewing a static optical load. Results are shown for a variety of proportional and integral term weights. Dashed lines show curves with various proportional term gains while the integral term is held at a constant weighting of 190 data units. Similarly, dotted lines mark curves with various integral term weights while the proportional term is held at a constant gain of 1 091 data units.

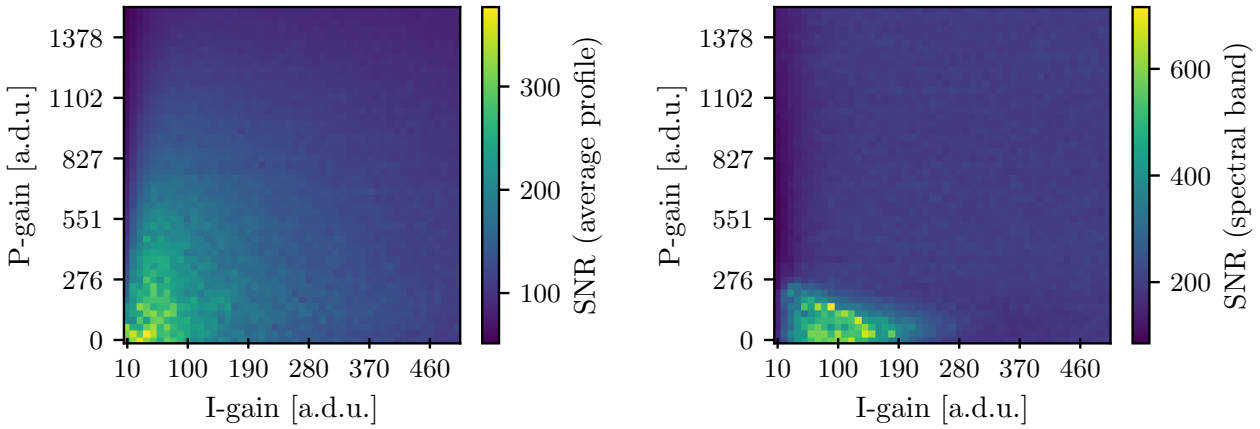

Figure 10. The effect of varying proportional and integral-term gains on the SNR of central detector measurements of a 90°C blackbody source chopped at 40 Hz. The left panel shows SNR measurements that compare the amplitude of the average chopped signal profile to noise measured in the full detector frequency band (average profile SNR). The right panel demonstrates similar measurements in which SNR has been estimated comparing the spectral peak corresponding to the modulated optical load to noise within the same frequency band (spectral band SNR).

Table 2. Detector parameters that we have determined to provide a better-optimised central detector for the DFI testbed are shown with the default parameters. Selected detector performance metrics are also shown.

Detector Parameter	Default	Optimised
Pulse width [loop counts]	10	12
Blanking time [loop counts]	4	6
Read index [loop counts]	9	11
Setpoint [a.d.u.]	10 000	9 500
P-gain [a.d.u.]	1 000	600
I-gain [a.d.u.]	200	150
D-Gain [a.d.u.]	0	0
Detector time constant [ms]	0.96 ± 0.06	1.65 ± 0.01
Detector array framerate [kHz]	12.913	11.106

The spectral NEP of the DFI can be expressed using the expression for a nominal FTS,

$$\mathrm{NEP}_{\mathrm{FTS}} = \varsigma \sqrt{\frac{\Delta\sigma}{2v_{\mathrm{stage}}}} \quad [\mathrm{W}/\sqrt{\mathrm{Hz}}], \tag{5}$$

where $\varsigma\,[\mathrm{W/cm^{-1}}]$ represents spectral noise, $v_{\mathrm{stage}}\,[\mathrm{cm/s}]$ is the scanning speed of the double-rooftop mirrors of the DFI (in units of optical path difference), and $\Delta\sigma\,[\mathrm{cm^{-1}}]$ is the spectral resolution.[23,24] To determine spectral noise, we have considered 200 spectral scans of the DFI and subtracted the average spectrum from each single-scan spectrum. Assuming that the noise amplitudes of each scan are statistically independent, the total spectral noise is determined from the quadrature sum of the noise from each scan ($\varsigma^2 = 1/N^2 \sum_i^N \varsigma_i^2$). Fig. 13 compares spectral noise in the central detector obtained from spectral measurements (in units of raw detector signal) of a blackbody source at 1100°C using the default detector parameters set by QMC Instruments and measurements using the optimised parameters. Fig. 14 shows the corresponding $\mathrm{NEP}_{\mathrm{FTS}}$ from each spectral noise measurement. For details on the spectral calibration of the DFI, see Benson et al. (2023)[17] and Benson (2024).[14] The optimised detector parameters result in a 37–79% reduction in noise throughout the spectral band of the DFI (i.e., improving spectral noise by a factor of 1.6–4.8).

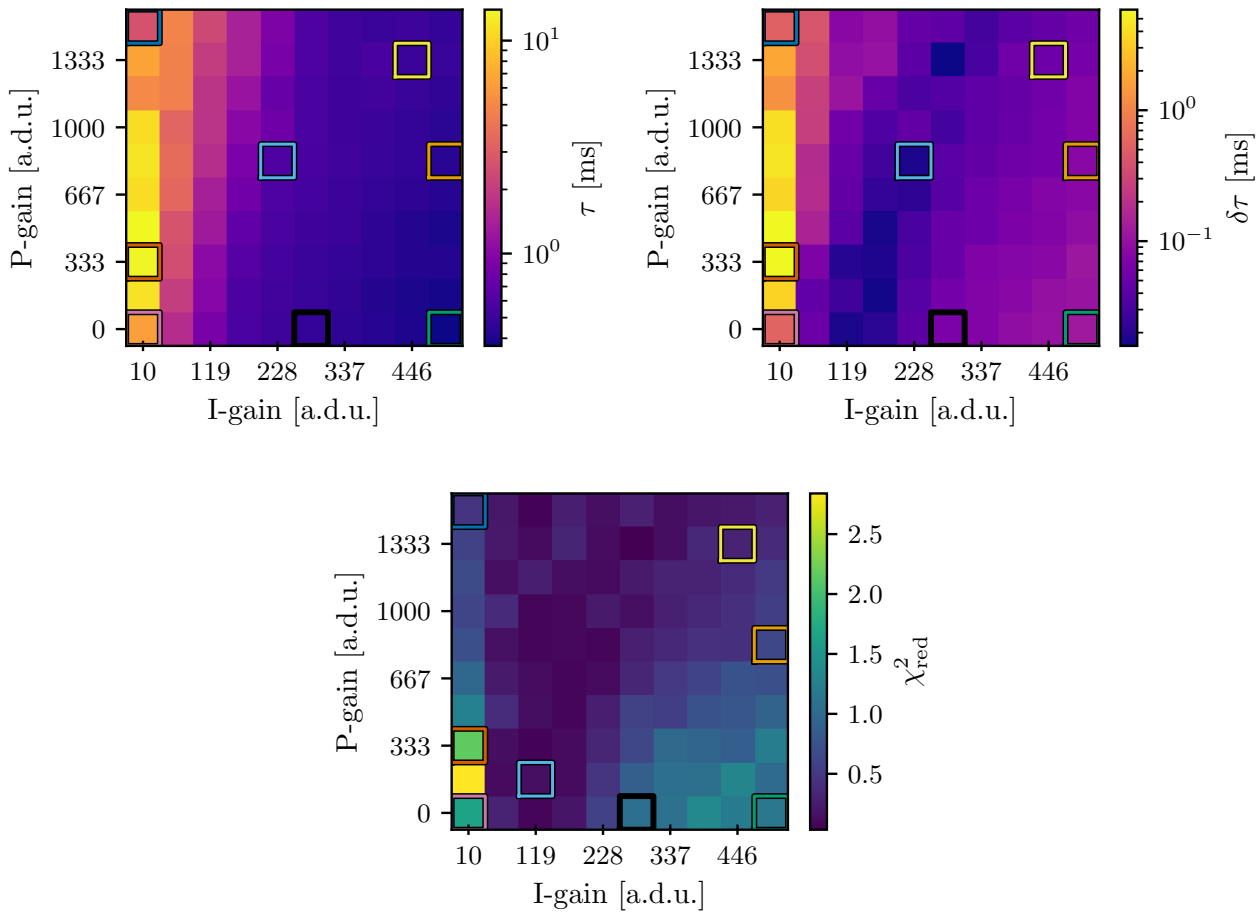

Figure 11. The effective time constant (upper-left) and associated uncertainty (upper-right) of the central detector under different P and I term weighting in its PID control. Each time constant value is determined from a least-squares fit to the response of the detector to a photomixer source that has been modulated with a chopper wheel. The value of χ^2_{red} as a goodness of fit metric for the time constant measurements of the central detector is shown in the lower panel. Cases that demonstrate irregular detector response profiles and more typical behaviour are outlined by a coloured square. Their response profiles are shown in Fig. 12.

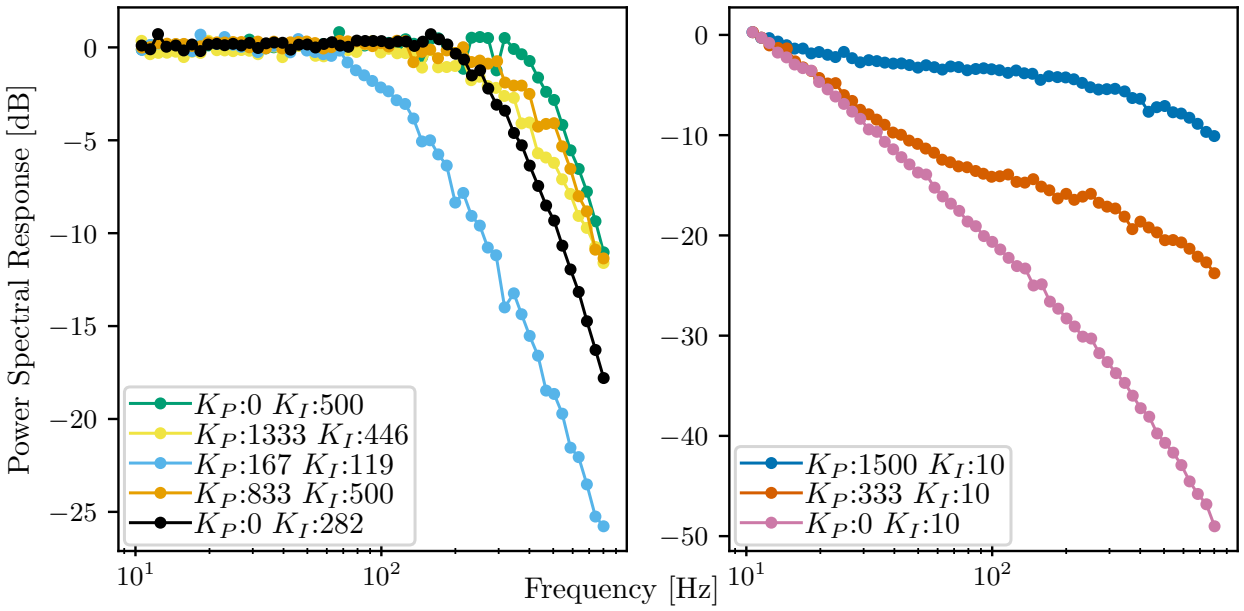

Figure 12. The response of the central detector corresponding to particular P and I gain conditions of interest denoted in Fig. 11. Response measurements with an I gain of 10 (right panel) show non-linear behaviour prior to the high-frequency cutoff. These are shown in the right panel while more typical responses are shown in the left.

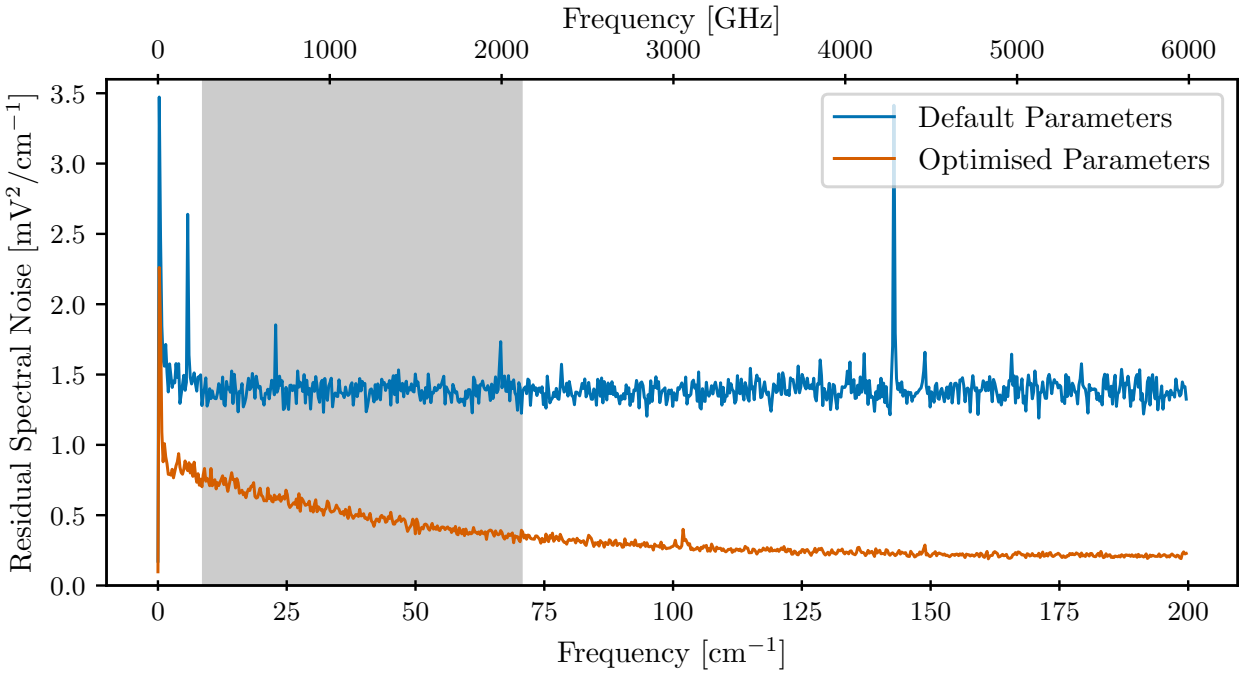

Figure 13. The spectral noise measured by the FTS while viewing a blackbody source with the default parameters set by QMC Instruments and with the optimised parameters. The region shaded in grey marks the spectral bandpass of the DFI.

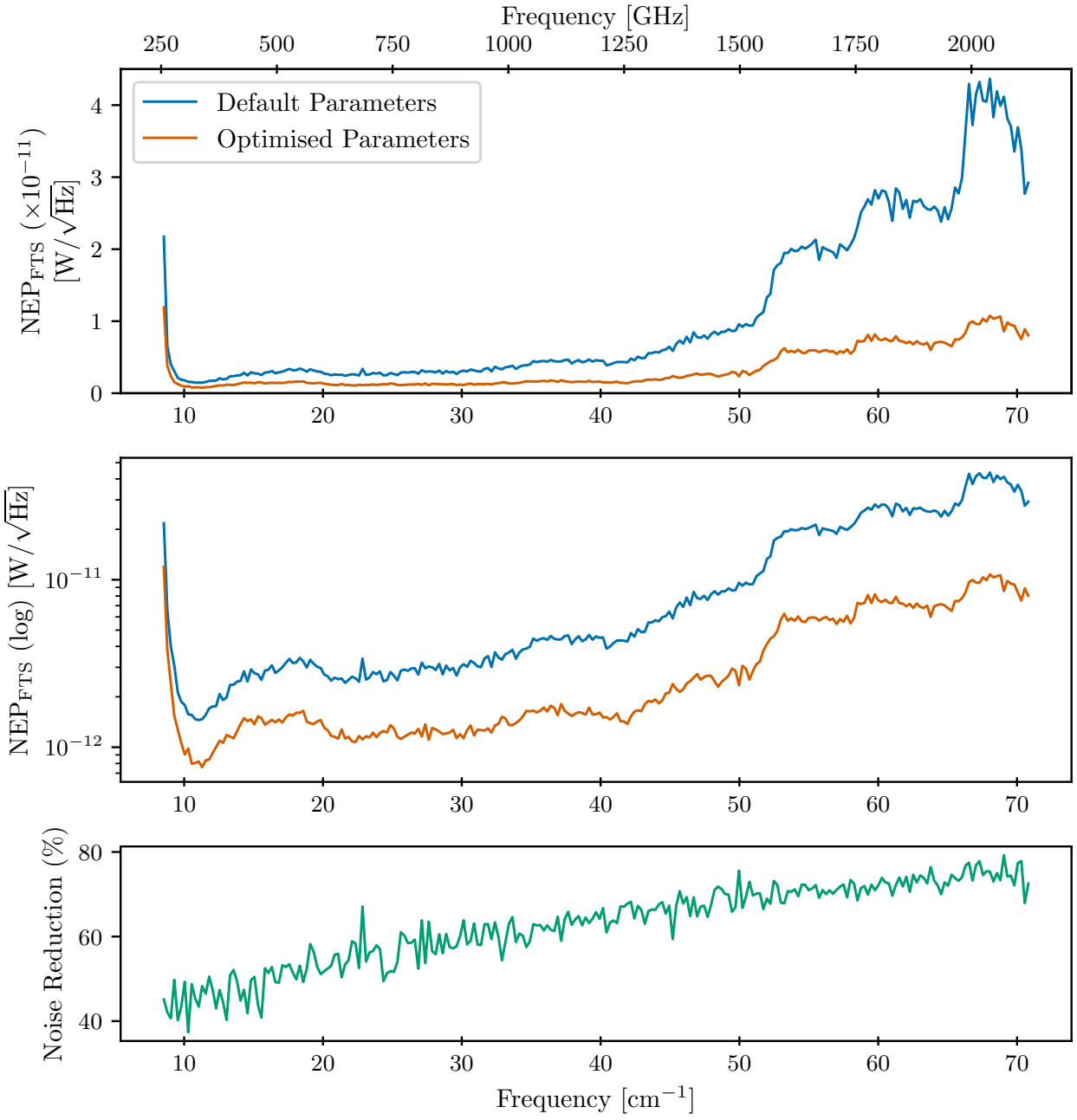

Figure 14. The spectral NEP of the central detector in the DFI testbed using default and optimised detector parameters. These measurements correspond to the spectral noise shown in Fig. 13.

3. CONCLUSIONS AND FUTURE WORK

The PID feedback-controlled array of TES bolometers that we have studied is a versatile system that can be optimised through the tuning of its PID feedback loops and adjusting the timing of its multiplexing process. Through in situ measurements of the superconducting transitions of the detector array, we have determined the optimal operational setpoints for the PID feedback of each detector. Additionally, we have measured the dynamic thermal conductance of the central detector to be $0.22 \pm 0.01\,\mu$W/K when operating about its optimal setpoint.

By modifying the timing of the multiplexing process and the PID tuning of the central detector, we have better optimised the central detector for use in the DFI testbed. This optimisation requires the noise performance of the detector to be balanced with the speed required to effectively measure interference from the DFI. Our efforts have resulted in a 37–79% reduction in the noise of spectral measurements made with the DFI. This noise reduction can conceivably reduce the time required to achieve sufficient SNR in full spatial/spectral measurements from greater than 12 hours to ∼6-8.

Early investigations into the effectiveness of step-and-integrate observations with the DFI have been found to suffer from low-frequency noise in the detectors, as would be expected without external modulation.[14] We have shown in this work that superior noise performance of the central detector is obtained with PID tuning that results in a relatively slow detector response. Effective measurements made with the DFI using the rapid-scanning technique require that optical modulation from the interferometer at the lowest spectral frequency be above the detector signal band that is dominated by low-frequency noise while also having a detector time constant that is sufficiently fast to measure the optical modulation from the highest spectral frequency band (see Equation 4). Should a step-and-integrate technique coupled with optical modulation from an external source (such as a mechanical chopper) be employed, the detector time constant need only be sufficient to measure the set modulation frequency. In principle, this could be as low as ∼5 Hz. Based upon our measurements of detector performance with PID and multiplex timing parameters corresponding to a detector time constant tuned for measuring ∼5 Hz modulation, we anticipate this step-and-integrate arrangement has the potential to modestly improve the SNR of interferometer by a further factor of ∼1.5.

While the focus of our efforts with the DFI testbed has been to demonstrate its capabilities as a spatial and spectral interferometer, the ultimate goal is to also leverage the wide-field capabilities of the DFI as an imaging spectrometer. In anticipation of this, the optimisation of the full detector array should be investigated. Using the methodology and informed by the measurements presented here, we are extending the optimisation process for the full array of 25 detectors.

ACKNOWLEDGMENTS

This development is supported by Canada Research Chairs (CRC), Canada Foundation for Innovation (CFI), Alberta Research Capacity Program (RCP), Alberta Innovates (AI), and Natural Science and Engineering Research Council of Canada (NSERC) grants. We acknowledge CMC Microsystems and Canada's National Design Network (CNDN). We would like to acknowledge Mr. Vincent Weiler, Mr. Manimeldura Dinula De Silva, Mr. Himadri Saha, Mr. Klondike Taylor, and Ms. Yuxin Zhai for their contributions to laboratory infrastructure which made this work possible.

REFERENCES

[1] R. Hill, K. W. Masui, and D. Scott, "The Spectrum of the Universe," *Applied Spectroscopy* **72**, 663–688 (2018).

[2] F. P. Helmich and R. J. Ivison, "FIRI—A far-infrared interferometer," *Experimental Astronomy* **23**, 245–276 (2009).

[3] D. Farrah, K. E. Smith, D. Ardila, *et al.*, "Review: far-infrared instrumentation and technological development for the next decade," *Journal of Astronomical Telescopes, Instruments, and Systems* **5**, 020901 (2019).

[4] M. Harwit, D. Leisawitz, and S. Rinehart, "A far-infrared/submillimeter kilometer-baseline interferometer in space," *New Astronomy Reviews* **50**(1), 228–234 (2006). First Light and Reionization: Theoretical Study and Experimental Detection of First Luminous Sources in the Universe.

[5] N. R. Council *et al.*, *Astronomy and astrophysics in the new millennium*, National Academies Press, Washington DC (2001).

[6] D. Leisawitz, C. Baker, A. Barger, *et al.*, "The space infrared interferometric telescope (SPIRIT): High-resolution imaging and spectroscopy in the far-infrared," *Advances in Space Research* **40**, 689–703 (2007).

[7] A. Lyngvi, J. M. P. Armengol, A. Barton, *et al.*, "Far infrared interferometer technology reference study," in *57th International Astronautical Congress*, A3–1 (2006).

[8] G. Bignami and E. S. Agency, *Cosmic vision: Space science for Europe 2015–2025*, ESA Publications Division (2005).

[9] D. Schito, S. Pezzuto, and W. Holland, "Far Infra-red Space Intereferometer Critical Assessment:definition/update of key science questions and relevant data products," tech. rep. (2014). Last Editor: L. Spinoglio.

[10] H. Linz, H. Beuther, M. Gerin, *et al.*, "ESA Voyage 2050 White Paper bringing high spatial resolution to the Far-infrared–A giant leap for astrophysics," *arXiv preprint arXiv:2002.06693* (2020).

[11] P. L. Richards, "Bolometers for infrared and millimeter waves," *Journal of Applied Physics* **76**, 1–24 (1994).

[12] K. D. Irwin and G. C. Hilton, "Transition-edge sensors," *Cryogenic particle detection* , 63–150 (2005).

[13] P. D. Mauskopf, "Transition Edge Sensors and Kinetic Inductance Detectors in Astronomical Instruments," *PASP* **130**, 082001 (2018).

[14] C. S. Benson, *Feedback-Controlled Transition Edge Sensor Bolometers in a Far-Infrared Double-Fourier Interferometer*. PhD thesis, University of Lethbridge (2024).

[15] L. D. Spencer, R. V. Sudiwala, C. S. Benson, *et al.*, "Optimization of a cryogenic transition-edge sensor detector array for far-infrared astrophysics," in *Space Telescopes and Instrumentation 2022: Optical, Infrared, and Millimeter Wave*, **12180**, 1018–1035, SPIE (2022).

[16] J. Scott, C. Benson, and L. Spencer, "Design, operation, and characterization of a laboratory spatial-spectral Fourier transform interferometer," *IEEE Transactions on Terahertz Science and Technology* **13**(6), 636–644 (2023).

[17] C. S. Benson, J. P. Scott, and L. D. Spencer, "Detector performance and characterization in a double-Fourier interferometry testbed," in *Optica Sensing Congress 2023 (AIS, FTS, HISE, Sensors, ES)*, *Optica Sensing Congress 2023 (AIS, FTS, HISE, Sensors, ES)* , JW2A.24, Optica Publishing Group (2023).

[18] G. C. Jaehnig, K. Arnold, J. Austermann, *et al.*, "Development of Space-Optimized TES Bolometer Arrays for LiteBIRD," *Journal of Low Temperature Physics* **199**, 646–653 (2020).

[19] K. Rostem, D. M. Glowacka, D. J. Goldie, *et al.*, "Thermal conductance measurements for the development of ultra low-noise transition-edge sensors with a new method for measuring the noise equivalent power," in *Millimeter and Submillimeter Detectors and Instrumentation for Astronomy IV*, W. D. Duncan, W. S. Holland, S. Withington, *et al.*, Eds., **7020**, 70200L, International Society for Optics and Photonics, SPIE (2008).

[20] S. P. Davis, M. C. Abrams, and J. W. Brault, *Fourier transform spectrometry*, Elsevier (2001).

[21] L. D. Spencer, D. A. Naylor, B. M. Swinyard, *et al.*, "A Fourier transform spectrometer for ground testing of the Herschel/SPIRE instrument," in *Optical, Infrared, and Millimeter Space Telescopes*, J. C. Mather, Ed., *Society of Photo-Optical Instrumentation Engineers (SPIE) Conference Series* **5487**, 501–512 (2004).

[22] A. J. Deninger, A. Roggenbuck, S. Schindler, *et al.*, "2.75 THz tuning with a triple-DFB laser system at 1550 nm and InGaAs photomixers," *Journal of Infrared, Millimeter, and Terahertz Waves* **36**, 269–277 (2015).

[23] L. D. Spencer, *Imaging Fourier transform spectroscopy from a space based platform: the Herschel/SPIRE Fourier transform spectrometer*. PhD thesis, University of Lethbridge (2009).

[24] E. Serabyn and E. W. Weisstein, "Fourier Transform Spectroscopy of the Orion Molecular Cloud Core," *Astrophysical Journal* **451**, 238 (1995).